Chemical Engineering Journal 481 (2024) 148399

Contents lists available at ScienceDirect

Chemical Engineering Journal

journal homepage: www.elsevier.com/locate/cej

Enhancing plasma-catalytic toluene oxidation: Unraveling the role of Lewis-acid sites on δ-MnO_2

Zheng Bo [a], Mengyu Cao [a], Huihui Zhang [a], Yaolin Wang [b], Jianhua Yan [a,*], Kefa Cen [a], Kostya (Ken) Ostrikov [c], Xin Tu [b,*]

[a] State Key Laboratory of Clean Energy Utilization, Institute for Thermal Power Engineering, College of Energy Engineering, Zhejiang University, Hangzhou, Zhejiang Province, 310027, China
[b] Department of Electrical Engineering and Electronics, University of Liverpool, Liverpool L69 3GJ, UK
[c] School of Chemistry and Physics, Centre for Materials Science, Centre for Clean Energy Technologies and Practices, and Centre for Waster Free World, Queensland University of Technology (QUT), Brisbane, Queensland 4000, Australia

ARTICLE INFO

Keywords:
Plasma catalysis
Volatile organic compounds
Toluene oxidation
δ-MnO_2
Lewis-acid site
Oxygen vacancies

ABSTRACT

The emission of volatile organic compounds (VOCs) into the air, primarily due to human activities, has caused significant environmental pollution and health concerns. In response, the development of advanced environmental catalysts is crucial, and δ-MnO_2 has emerged as a promising material for efficient VOC oxidation. However, the identification of the specific active sites and the underlying oxidation mechanisms of this material remain unclear, hindering the development and optimization of high-activity catalysts. Herein, we present a strategy to remove the internal water and hydrated cations from δ-MnO_2, thereby unblocking the inter-lamellar gaps and exposing the internal Lewis-acid sites, while maintaining other physical and chemical characteristics of the sample unchanged. Notably, the well-defined δ-MnO_2 catalysts with more accessible interlayer Lewis-acid sites exhibited significantly enhanced catalytic activity in toluene oxidation, demonstrated in both two-stage plasma catalysis and single-stage ozonation processes. A quantitative analysis of Lewis-acid sites and initial toluene reaction rates revealed that these Lewis-acid sites serve as the active centers for toluene adsorption and activation, and the heterogeneous reaction between toluene and ozone follows the Langmuir-Hinshelwood mechanism. Moreover, in-depth analysis of byproducts showed that δ-MnO_2 rich in Lewis-acid sites promoted the oxidation of intermediates, such as esters, hydrazides, and ketones, leading to a more complete toluene oxidation. This work not only fully explores the potential of δ-MnO_2 as a catalyst, but also provides valuable insights into the elucidation of unknown catalytic active sites, potentially paving the way for the rational design of more efficient catalysts for VOC oxidation.

1. Introduction

Volatile organic compounds (VOCs) are a major source of air pollution, contributing to the formation of photochemical smog, secondary aerosols, and increasing ozone levels [1]. The development of effective VOC removal technologies is crucial for improving air quality and protecting public health. The strong oxidation ability of ozone (O_3) at ambient temperatures has made it a promising strategy for VOC removal, and its catalytic oxidation has attracted increasing interest [2–5]. Non-thermal plasma (NTP) is a promising technology for VOC removal due to its ability to generate both ozone and active species (including excited species and radicals) that effectively decompose VOCs [2,6]. This synergy is further enhanced in a two-stage plasma catalysis system, where NTP acts as a pre-treatment step to partially decompose the VOCs. This pre-treatment enhances the efficiency of the subsequent catalytic ozonation of the unreacted VOC molecules and reaction intermediates, allowing for complete degradation of the VOCs. This two-stage approach offers several advantages over conventional technologies, including reduced ozone consumption, enhanced catalyst selectivity, lower energy consumption, and broader VOC removal range. Importantly, the activity of the post-placed catalyst plays a pivotal role in achieving superior VOC decomposition and mineralization [6].

Among the widely reported catalysts, MnO_2, particularly δ-MnO_2, has emerged as the most promising catalyst for the conversion of ozone

* Corresponding authors.
E-mail addresses: yanjh@zju.edu.cn (J. Yan), xin.tu@liverpool.ac.uk (X. Tu).

https://doi.org/10.1016/j.cej.2023.148399
Received 14 September 2023; Received in revised form 9 December 2023; Accepted 26 December 2023
Available online 27 December 2023

and VOCs [4,7–9]. δ-MnO_2 with a unique 2D layer lattice structure and interlayer spacing of ~ 7.1 Å could be more favorable for mass transfer and catalyst-reactant contact compared to other MnO_2 phases, including α-, β-, and γ-MnO_2, which exhibit 1D tunnels with dimensions of approximately 2.3 × 2.3 Å or 2.3 × 4.6 Å [8,10]. Second, the conversion of ozone on a catalyst is generally attributed to oxygen vacancies, where ozone can be converted to reactive oxygen species (e.g., O^{2-} and O_2^{2-}) for further oxidation of VOCs and their fragments [4,11]. Zeng et al. demonstrated that δ-MnO_2 exhibits the highest concentration of oxygen vacancy (V_O) among all MnO_2 phases [4], making it an ideal catalyst for efficient ozone activation and enhanced oxidation ability. Recognizing the crucial role of oxygen vacancies, significant efforts have been dedicated to increasing the number of oxygen vacancies on the catalyst surface, such as crystallinity modulation [9], doping [12,13], layer exfoliation [14], heterostructure customizing [15,16], ball milling etc. [17]. However, simply increasing oxygen vacancies alone may not be the most effective approach to enhance the performance of δ-MnO_2 due to fundamental limitations arising from the interplay between oxygen vacancy content, the Mn^{3+}/Mn^{4+} ratio on the MnO_2 surface, and the specific surface area of the catalyst [4]. Moreover, it remains unclear whether increasing oxygen vacancies and ozone conversion is the only way to enhance VOC ozonation.

Recently, Wei et al. demonstrated that VOC (e.g., toluene) ozonation over MnO_2 catalysts follows the Langmuir-Hinshelwood (L-H) mechanism [18–20]. Under this mechanism, only VOC molecules that are chemically adsorbed on specific active sites can react with reactive oxygen species (ROS) generated from ozone at the oxygen vacancies. Since oxygen vacancies have been established as the active sites for ozone adsorption and conversion [4], identifying and tuning the as yet unknown sites for VOC adsorption and activation becomes critical to enhance the performance of the δ-MnO_2 catalyst in ozone-assisted catalytic VOC oxidation. Previous studies have identified Lewis-acid sites, which are coordinately unsaturated metal atoms situated on the surfaces of transition metal oxides adjacent to oxygen vacancies [21,22], suggesting that these sites may synergistically cooperate with oxygen vacancies to promote VOC adsorption and subsequent oxidation. Moreover, the first step in VOC oxidation on metal oxide catalysts involves the transfer of an electron from VOCs to the metal oxide, followed by the release of a proton from a methyl group (e.g., methyl of toluene). Notably, Lewis-acid sites can only function as electron acceptors [23]. These findings suggest that Lewis-acid sites may be the active sites for catalytic oxidation of VOCs. Recent studies have established a connection between the concentration of acid sites in a catalyst and its adsorption/oxidation activity of VOCs [24,25]. However, earlier experiments were unable to isolate acid site concentration as a unique variable; attempts to enhance acidity often inadvertently altered multiple factors (e.g., morphology, crystallinity, chemical properties, oxygen vacancy content, and surface area), hindering the identification of the actual active sites. Therefore, we believe that fine-tuning the density and activity of Lewis-acid sites while controlling the reaction parameters can be a promising and effective method to determine the exact toluene adsorption/activation sites.

Herein, we have developed a two-stage plasma catalysis system for the oxidation of toluene. Toluene was selected as a model VOC due to its ubiquity, representative structure, and potential to shed light on the degradation mechanisms of broader VOC classes. We synthesized δ-MnO_2 using a simple ion-exchange reaction between Mn-MIL-100 (a type of metal organic framework (MOF)) and hydroxyls in an alkali solution. Compared to the conventional hydrothermal method for δ-MnO_2 synthesis [4], our method allowed for the preparation of δ-MnO_2 samples with a larger specific surface area and a more porous structure. More importantly, we employed acid and heat treatment to remove hydrated Na cations in the layer (e.g., $[Na(H_2O)_4]^+$) [26], providing δ-MnO_2 with unobstructed channels through which toluene can diffuse and be adsorbed onto the inner Lewis-acid sites. In addition, we used pyridine to cap and deactivate the Lewis-acid sites as a control group since pyridine can coordinate with unoccupied orbitals of transition metals, effectively neutralizing the catalytic activity of the Lewis-acid sites [27]. Using these δ-MnO_2 catalysts with varying accessibility to Lewis-acid sites, we conducted catalytic ozone conversion, plasma-catalytic toluene conversion, and toluene adsorption reactions. The conversion of toluene in the presence of water vapor was also evaluated. To quantitatively analyze the relationship between Lewis-acid sites and toluene conversion, we further performed one-step catalytic ozonation of toluene, excluding the influence of plasma on toluene conversion. Additionally, the role of Lewis-acid sites in the oxidation of organic intermediates, which is related to the complete oxidation of toluene, was investigated through byproduct analysis. Finally, a plausible toluene degradation pathway by δ-MnO_2 was proposed, considering the presence of its interlayer Lewis-acid sites, which are beneficial for catalytic activity.

2. Experimental

2.1. Synthesis of δ-MnO_2

To prepare δ-MnO_2, Mn-MIL-100 was first synthesized via a hydrothermal reaction between trimesic acid and manganese nitrate (Mn$(NO_3)\cdot 4H_2O$). Specifically, manganese nitrate ($Mn(NO_3)_2\cdot 4H_2O$, 2 mmol, Aladdin) and trimesic acid (H_3BTC, 1.9 mmol, Aladdin) were dissolved in ethanol (18 mL, Aladdin) under ultrasonic conditions to form a clear solution [28]. The clear reaction solution was then transferred into a Teflon-lined steel autoclave and heated at 125 °C for 2 h. After cooling to room temperature, the brown product was obtained by centrifugation and washed three times with ethanol. The resulting solid was vacuum dried overnight at 70 °C. Following that, 1.2 g of the as-synthesized Mn-MIL-100 was dispersed in 400 mL NaOH solution (0.04 M) under electromagnetic stirring at ambient temperature and pressure. After 10 h reaction, the suspension was centrifuged with deionized water and ethanol for three times, respectively, and then vacuum dried at 70 °C overnight to obtain the dark brown δ-MnO_2 powder. This synthesis represents a novel approach to use MOFs as precursors for the preparation of δ-MnO_2 material.

2.2. Synthesis of acid-MnO_2, annealed-MnO_2, and cap-MnO_2

Hydrated Na cations unclogging the channels between the lattice layers of δ-MnO_2 were removed by simple acid washing or annealing. In brief, δ-MnO_2 was mixed with 0.2 M HNO_3 solution in a mass ratio of 1:20 and stirred at room temperature for 4 h. The mixture was then centrifugally washed with deionized water for 6 times. After that, the obtained precipitate was dried overnight at 150 °C in a vacuum oven and labelled as acid-MnO_2. As hydrated cations are unstable and easily dehydrated, annealing treatment was carried out in an argon atmosphere at 200 °C in a tube furnace for 4 h, and the resulting catalyst was annealed-MnO_2. Furthermore, to cap the Lewis-acid sites, pristine δ-MnO_2 with 0.1 mL pyridine was placed in a vacuum drying oven at 100 °C and 3–4 Pa for 30 min, ensuring δ-MnO_2 adsorbed pyridine until saturation. The resulting pyridine-saturated δ-MnO_2 with deactivated Lewis-acid sites was cap-MnO_2.

2.3. Catalysts characterization

A scanning electron microscope (SEM, SU-8010, Hitachi) was used to evaluate the morphologies of δ-MnO_2, acid-MnO_2 and annealed-MnO_2. High-resolution transmission electron microscopy (HRTEM, HT-7700, Hitachi) was used to examine microstructures of the samples. The crystalline structures of the catalysts were measured by X-ray diffraction (XRD, X'Pert power, PANAlytical B.V.) and Raman spectroscopy (Renishaw inVia). The Brunauer-Emmett-Teller (BET) surface area and Barrett-Joyner-Halenda (BJH) pore-size distribution were investigated by N_2 sorption isotherms (Autosorb iQ Station 1). Additionally, CO_2

sorption isotherms were used to analyze the microporous structures of the catalysts (Micromeritics ASAP 2460). The electron paramagnetic resonance (EPR) spectra were collected on a Bruker EMX PLUS spectrometer to investigate oxygen vacancies. The chemical properties of the δ-MnO_2 catalysts were confirmed by X-ray photoelectron spectroscopy (XPS, XR3E2, VG Escalab Mark II) with Al Kα radiation (1486.6 eV), and all the binding energies were calibrated by referencing the C 1 s peak at 284.6 eV. The sodium content of the catalysts was determined using inductively coupled plasma (ICP, Thermo Fisher iCAP PRO) spectroscopy. The removal of water from the catalysts was analyzed by thermogravimetric analysis/mass spectrometry (TG-MS, TG: Netzsch STA 449 F3, MS: QMS403D). The acidity of the δ-MnO_2 catalysts was measured using temperature-programmed desorption of ammonia (NH_3-TPD) and pyridine adsorption IR spectra (Py-IR, PE FT-IR Frontier). For NH_3-TPD, 0.2 g of the sample was exposed to a stream of ammonia gas (50 mL/min) at 100 °C for 1 h. The sample was then held at 100 °C for an additional 2 h with a stream of argon gas (50 mL/min) to remove any physically adsorbed ammonia molecules. The sample was then heated up to 400 °C at a rate of 10 °C/min. For Py-IR, 0.2 g of the sample was vacuum-treated at room temperature for 1 h to record the background. The sample was then exposed to pyridine-saturated vapor for 30 min. Finally, the sample was heated up to 100 °C at a rate of 10 °C/min to induce pyridine desorption.

2.4. Reactor setup and experimental procedures

As shown in Fig. S1, the plasma catalysis system for toluene oxidation consisted of a gas supply unit, a coaxial dielectric barrier discharge (DBD) reactor, a packed-bed catalytic reactor, and a product analysis unit. The DBD reactor contained a quartz tube (external diameter of 8 mm and inner diameter of 6 mm), a high voltage electrode (a stainless-steel rod with a diameter of 4 mm placed coaxially in the quartz tube) and a ground electrode (a 10 mm-long copper mesh grounded and wrapped around the quartz tube). The high voltage electrode was connected to a high voltage power supply (CTP-2000 K, Suman Plasma Technology), and the specific input energy (SIE) was varied from 131 to 288 J/L at a fixed frequency of 9.6 kHz. The applied voltage and current signals were recorded using a digital oscilloscope (MDO 3034, Tektronix), and the discharge power was calculated using the Lissajous figure method (see Fig. S2). The fixed-bed catalyst reactor was placed after the DBD reactor, forming a two-stage plasma catalysis configuration. In the catalytic reactor, a mixture of 200 mg catalyst and 2 g quartz sand was packed and fixed by quartz wool without any external heating.

Three catalytic processes were investigated using this two-stage plasma catalysis system: ozone conversion, toluene decomposition (i.e., toluene conversion using NTP combined with catalyst) and toluene ozonation (i.e., toluene conversion using catalyst alone). In the ozone conversion experiment, air was controlled by a mass flow controller (D08-3F, Sevenstars) and passed through the DBD reactor and then the catalyst bed. To determine whether the presence of toluene and its intermediates affects ozone generation and its subsequent catalytic conversion, toluene was mixed with air before NTP as a control group. An ozone monitor (Model 106-MH, 2B Technology) was used to measure ozone generated by the DBD reactor and that remained after the catalytic reactor. Note that the retention rate of pyridine adsorbed on Lewis-acid sites (the retention of the cap effect) was also examined in this experiment, and the details can be found in Fig. S3. In the toluene decomposition experiment, air was mixed with toluene before flowing into to the DBD reactor. A high-resolution syringe pump (LSP01-1BH, Longer Precision Pump) was combined with a toluene generator (FD-PG, Friend Laboratory Equipment) to produce a gas mixture containing 230 ppm of toluene vapor. Water vapor can be introduced and controlled using a water generator and a syringe pump. Furthermore, we investigated the individual effects of catalysts on toluene ozonation to better understand the role of Lewis-acid sites in the reaction. In this experiment, toluene was introduced after the DBD reactor. In contrast to the previously described two-stage plasma catalysis configuration, the DBD reactor in this case served only as an ozone generator, with toluene being converted only on the catalyst.

During these processes, toluene, CO, and CO_2 were measured online using a gas chromatograph (GC9790Plus, Fuli Instruments). Organic byproducts were collected using 20 mL of hexane solution with a 30-min adsorption time for GC-MS analysis (QP2010SE, Shimadzu). The NO_x (NO, NO_2, N_2O) generated by NTP and remained after the catalyst bed were measured using an online multi-component analyzer (Gasmet Dx4000, Finland). In addition, the Gasmet was also used to record toluene adsorption-penetration curves. Unless otherwise specified, all reactions were carried out with a 200 mg catalyst, a toluene concentration of 230 ppm, and a total gas flow rate of 0.5 L/min.

The specific input energy (SIE), ozone conversion (X_{ozone}), toluene conversion ($X_{toluene}$), CO_x selectivity (S_{COx}), energy yield (η_{EY}) and the initial reaction rates of toluene (r_{Tol}) are calculated using the following equations:

$$\mathrm{SIE}\left(\mathrm{J\ L^{-1}}\right) = \frac{P(\mathrm{W})}{Q(\mathrm{L\ s^{-1}})} \tag{1}$$

$$X_{\mathrm{ozone}}(\%) = \frac{C_{\mathrm{ozone-in}} - C_{\mathrm{ozone-out}}}{C_{\mathrm{ozone-in}}} \tag{2}$$

$$X_{\mathrm{toluene}}(\%) = \frac{C_{\mathrm{toluene-in}} - C_{\mathrm{toluene-out}}}{C_{\mathrm{toluene-in}}} \tag{3}$$

$$S_{\mathrm{COx}}(\%) = \frac{C_{\mathrm{CO2}} + C_{\mathrm{CO}}}{7 \times (C_{\mathrm{toluene-in}} - C_{\mathrm{toluene-out}})} \tag{4}$$

$$\eta_{\mathrm{EY}}\left(\mathrm{g\ kWh^{-1}}\right) = \frac{3.6 \times \mathrm{M} \times (C_{\mathrm{toluene-in}} - C_{\mathrm{toluene-out}})}{24.4 \times \mathrm{SIE}} \tag{5}$$

$$r_{\mathrm{Tol}}(\mu\mathrm{mol_{Tol}/g_{cat}{\cdot}s}) = \frac{Q \times (C_{\mathrm{toluene-in}} - C_{\mathrm{toluene-out}})}{24.4 \times m_{\mathrm{Cat}}} \tag{6}$$

where P is the discharge power calculated using the Lissajous method, and Q is the flow rate of the gas stream. $C_{ozone\text{-}in}$ and $C_{ozone\text{-}out}$ represent the concentration of ozone before and after the catalytic reactor, respectively. $C_{toluene\text{-}in}$ and $C_{toluene\text{-}out}$ are the inlet and outlet toluene concentrations, respectively. C_{CO2} and C_{CO} are the concentrations of generated CO_2 and CO, respectively. M denotes the molar mass of toluene. The weight of the catalyst used in one test is denoted by the symbol m_{Cat}. All errors are the result of three tests performed under the same conditions.

3. Results and discussion

3.1. Catalyst characterization

Fig. 1 shows the morphology and structural characteristics of the as-prepared catalysts. The pristine δ-MnO_2 exhibited flower-like nanosheets with a thickness of 5–10 nm (Fig. 1a). HRTEM images of the catalysts further revealed that these planar nanosheets were composed of several to tens of stacked lamellar lattices (Fig. 1b). The well-identified periodic lattice fringes of 7.1 Å closely matched the (0 0 1) facets of δ-MnO_2, confirming the proper synthesis of layered δ-MnO_2 [29]. The synthesis of δ-MnO_2 by mineralization of Mn-MIL-100 precursor in a basic medium can be considered an ion-exchange process between organic ligands in the MOF and hydroxyl radicals. Generally, OH^- groups penetrated into the interlayer open spaces of the Mn-MIL-100 and exchanged with organic ligands to form $Mn(OH)_2$. Since $Mn(OH)_2$ is highly unstable and can be easily oxidized [30], *in situ* oxidation of the $Mn(OH)_2$ intermediates proceeded simultaneously during the ion-exchange process. Notably, Na^+ cations were incorporated into the interlayer of the layered δ-MnO_2. Unlike δ-MnO_2 synthesized using conventional hydrothermal method [7], δ-MnO_2 prepared via this mild

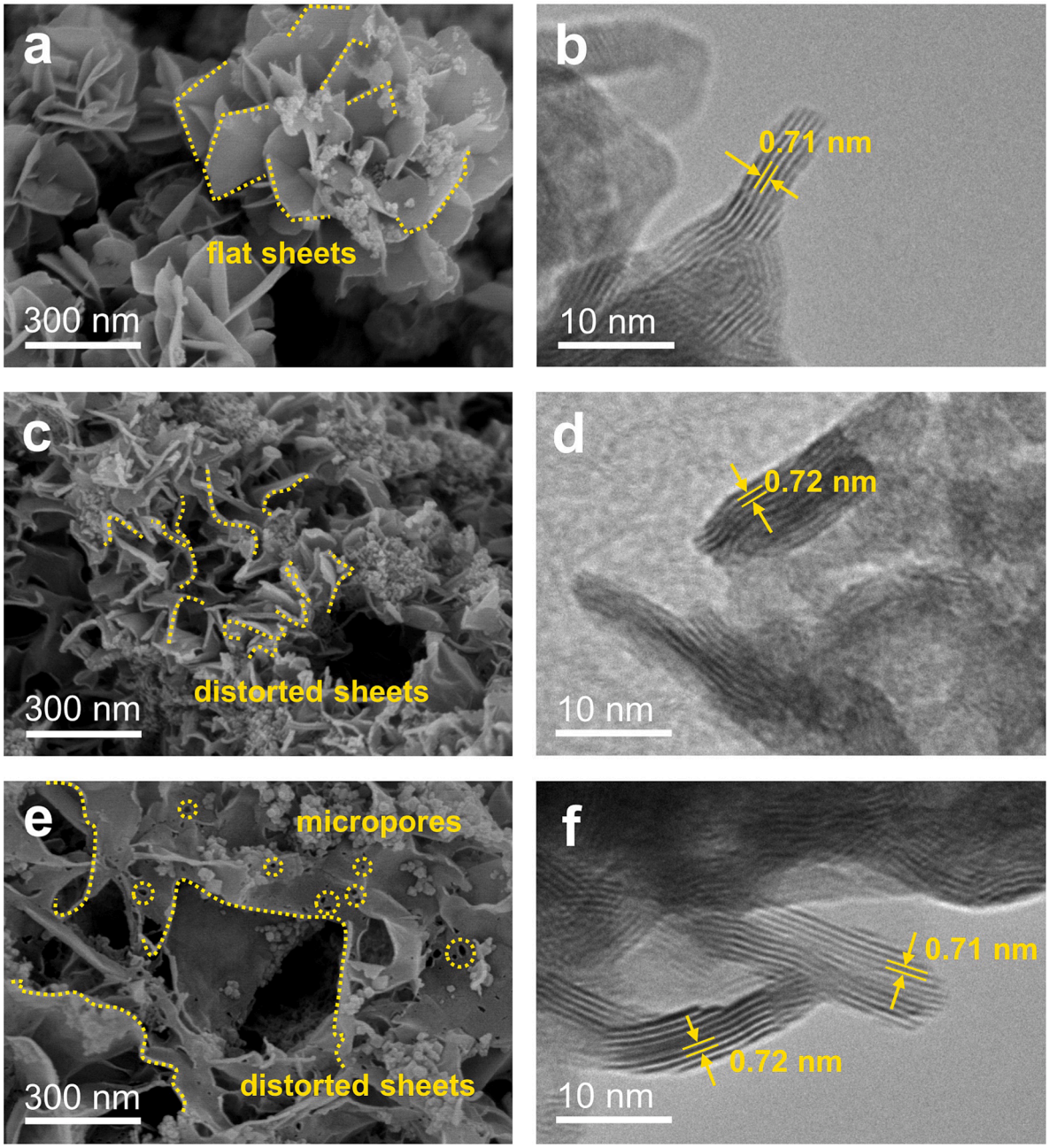

Fig. 1. Lamellar structure for engineering internal space for toluene ozonation revealed by electron microscopy. SEM and HRTEM images of δ-MnO_2 (a, b), acid-MnO_2 (c, d), and annealed-MnO_2 (e, f).

mineralization process avoided structural collapse and retained the porous structure of the Mn-MIL-100 template to a remarkable degree, as confirmed by subsequent BET characterization. Additionally, compared to 1D tunnels found in other MnO_2 phases, the 7.1 Å interlayer spacing in this well-organized δ-MnO_2 potentially enables unobstructed transport of reactant molecules [8]. Clearly, the acid treatment of the δ-MnO_2 did not alter the layered structure but induced a slight distortion of the nanosheets (Fig. 1c). The annealed-MnO_2 retained its 2D structure, albeit with the presence of pores on the nanosheets (Fig. 1e). Nonetheless, due to the open architecture of this material, these pores have a minimal impact on mass transfer. In addition, the HRTEM image (Fig. 1f) of the annealed-MnO_2 still shows the same lattice spacing (7.1–7.2 Å), which corresponds to the (0 0 1) facets of δ-MnO_2 [31].

The consistency in both the crystal and textural structures of the samples were further confirmed by XRD, Raman spectroscopy, N_2 sorption isotherms, and EPR. As shown in Fig. 2a, the three samples (i.e., δ-MnO_2, acid-MnO_2, and annealed-MnO_2) exhibited similar XRD patterns. Peaks at $2\theta = 12.5°$, 24.5°, 36.4°, and 65.6° correspond to the (0 0 1), (0 0 2), (1 0 0), and (1 1 0) planes of standard δ-MnO_2 (JCPDS, NO. 80–1098), respectively [29,31]. This result demonstrated proper preparation of δ-MnO_2 and indicated that no phase changes occurred following the annealing and acid treatment, which was consistent with the HRTEM results. In addition, the XRD results confirm that the sparse nanoparticles adhering to the nanosheets in the SEM images remained δ-MnO_2, despite their distinct morphology [32]. The Raman spectra also confirm the steady δ-sphere. As shown in Fig. 2b, the bands at ~573 cm^{-1} and ~645 cm^{-1} can be attributed to the symmetric stretching vibrations of Mn-O bonds within the MnO_6 octahedra, paralleled to and perpendicular to the basal (0 0 1) facet, respectively [14,15,33]. Therefore, the materials retain their identification as δ-MnO_2 even though the

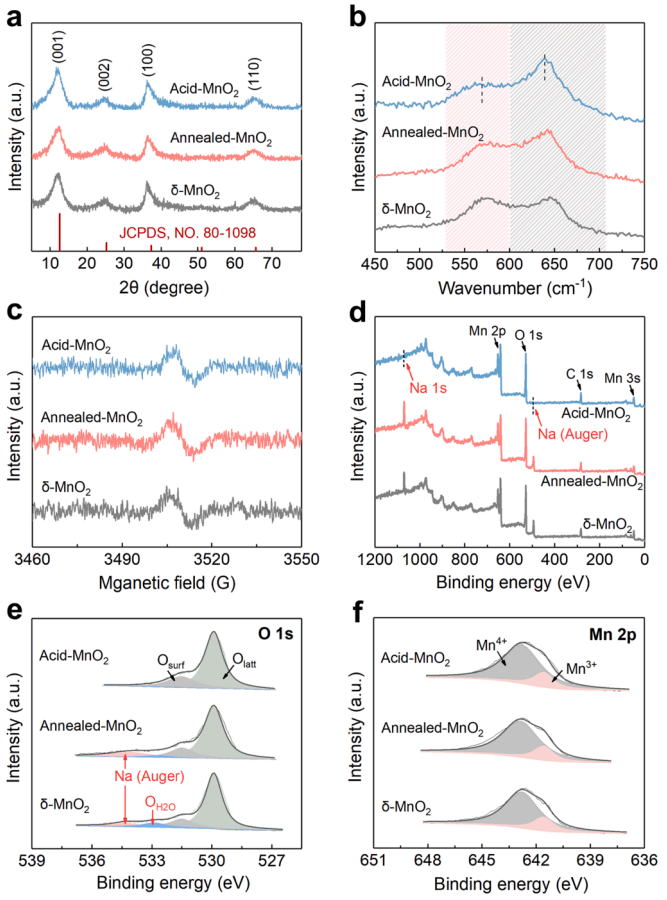

Fig. 2. Revealing the steady structural properties and the removal of structural water and hydrated Na^+ in the catalysts. (a) XRD patterns, (b) Raman spectra and (c) EPR spectra of δ-MnO_2, annealed-MnO_2, and acid-MnO_2. (d) XPS survey spectra, (e) XPS survey O 1s spectra and (f) Mn 2p spectra of the δ-MnO_2 catalysts.

relative intensities of these bands may vary. The band near 645 cm^{-1} of annealed-MnO_2 and acid-MnO_2 exhibits increased intensity and shifts towards lower wavenumbers compared to δ-MnO_2, indicating weakened layer interactions due to the relaxation of the confinement effect in the vertical direction [14]. Moreover, the band at ~573 cm^{-1} is slightly weaker in acid-MnO_2, possibly due to lattice distortion from acid treatment, which may slightly reduce crystal symmetry.

To investigate the potential active sites for toluene activation, it is important to maintain a consistent number of oxygen vacancies, which are known to facilitate ozone conversion. Using EPR spectroscopy, we performed a comprehensive analysis of oxygen vacancies in δ-MnO_2, annealed-MnO_2, and acid-MnO_2 catalysts. In Fig. 2c, all catalysts exhibit a symmetrical EPR signal at 3515 G with a g-factor of 2.003, corresponding to the unpaired electrons at the oxygen vacancies in δ-MnO_2 catalysts [7,34]. Similar signal intensities across all three samples suggest a comparable number of oxygen vacancies in each one. The XPS results further support the consistency of oxygen vacancies across the samples. As shown in Fig. 2e, the three peaks 529.9, 531.6, and 532.8 eV can be attributed to lattice oxygen (O_{latt}), surface oxygen species (O_{surf}), and adsorbed H_2O (O_{H2O}), respectively [9,34]. Given that the relative content of O_{surf} is directly linked to the abundance of surface oxygen vacancies [14], the slight increase in the O_{surf}/O_{latt} ratio observed in both annealed-MnO_2 and acid-MnO_2 catalysts suggests limited changes in the number of oxygen vacancies. Moreover, it is widely recognized that surface Mn^{3+} facilitates the formation of surface oxygen vacancies on MnO_2 [9,35]. Hence, the comparable Mn^{3+}/Mn^{4+} ratio (Fig. 2f and Table 1) confirms that the Vo remains stable (Peaks at 642.7 eV and 641.7 eV are attributed to Mn^{4+} and Mn^{3+}, respectively) [8].

Table 1
Na content and chemical states of O and Mn in δ-MnO_2, annealed-MnO_2, and acid-MnO_2.

Catalyst	Na content (wt %)	$O_{H2O}/O_{surf} + O_{latt}$ (%)	O_{surf}/O_{latt}	Mn^{3+}/Mn^{4+}
δ-MnO_2	3.95	9.5	0.20	0.22
Annealed-MnO_2	4.01	3.9	0.22	0.21
Acid-MnO_2	0.23	1.3	0.26	0.21

Despite the consistent morphologies and Vo intensities across the samples, a critical change that affects catalysis has occurred. As shown in Fig. 2d and e, peaks at 1071 eV, 494 eV, and 534.2 eV in the spectra of δ-MnO_2 and annealed-MnO_2 can be assigned to Na 1 s and Na Auger [36,37]. Notably, the absence of these Na peaks in the spectrum of acid-MnO_2 indicates the complete removal of Na cations from the interlayers. The removal of Na cations following acid treatment was also confirmed by ICP analysis, as evidenced by the sodium content values listed in Table 1. According to Lee et al., acid washing can remove cations from the lattice of materials due to the strong solubility power and higher reactivity of acids [38–40]. Hydrogen ions in the acid can participate in displacement reactions with the cations in the lattice, forming soluble metal salts. Moreover, the O 1s spectra (Fig. 2e) demonstrate a significant decrease in the water content of the δ-MnO_2 catalysts after both annealing and acid treatments. Notably, H_2O peaks at 532.8 eV are almost absent in the O 1s spectra of annealed-MnO_2 and acid-MnO_2, while a distinct H_2O peak is visible in the O 1s spectrum of δ-MnO_2. As summarized in Table 1, the relative adsorbed water content (in %) for δ-MnO_2, annealed-MnO_2, and acid-MnO_2 is determined as 9.5%, 3.9%, and 1.3%, respectively. Compared to δ-MnO_2, the relative water content of annealed-MnO_2 and acid-MnO_2 decreased by 64% and 88%, respectively. The TG-MS results further confirmed the removal of H_2O in annealed-MnO_2 and acid-MnO_2, as evidenced by the reduced weight loss and diminished H_2O signals during the programmed temperature elevation process (Fig. S4).

The gas sorption isotherms for the catalysts provided compelling evidence of limited morphological changes and the exposure of sub-nanometer interlayer spaces following annealing and acid treatments. As shown in Fig. 3a, the N_2 adsorption–desorption isotherms for δ-MnO_2, annealed-MnO_2, and acid-MnO_2 exhibit a high degree of similarity. All samples exhibit Type IV isotherm with an H3 hysteresis loop, confirming the consistent presence of mesoporous structures. The BET specific surface areas for δ-MnO_2, annealed-MnO_2, and acid-MnO_2 were comparable, with values of 245.2 m^2/g, 279.0 m^2/g, and 265.2 m^2/g, respectively (Table 2). The BJH pore size distributions obtained from the N_2 adsorption–desorption experiments were also nearly identical (Fig. 3b). Given that N_2 sorption isotherms provide precise measurements of the surface area for mesopores (2–50 nm) and macropores (>50 nm), it can be inferred that annealing and acid treatments have not significantly altered the morphology in the nanoscale. On the other hand, considering the limitations and potential inaccuracies of the BET method in measuring the specific surface area of microporous materials, we employed CO_2 instead of N_2 for a more accurate assessment of the specific surface area and pore size distribution within the sub-nanoscale space. As shown in Fig. 3c, the CO_2 adsorption–desorption intensity of annealed-MnO_2 and acid-MnO_2 exhibited a notable increase in the P/P_0 range of 0 to 0.025. Density functional theory (DFT) calculations reveal specific surface areas in the 0.35 to 0.7 nm pore range of 35.4 m^2/g for δ-MnO_2, 77.1 m^2/g for annealed-MnO_2, and 105.2 m^2/g for acid-MnO_2, an increase of 117.8% and 197.2%, respectively, due to annealing and acid treatments (Table 2). The CO_2-based pore size distribution further confirms the significant increase of sub-nanometer pores following annealing and acid treatments (Fig. 3d). The notable increase in sub-nanometer space is undoubtedly due to the removal of blockages

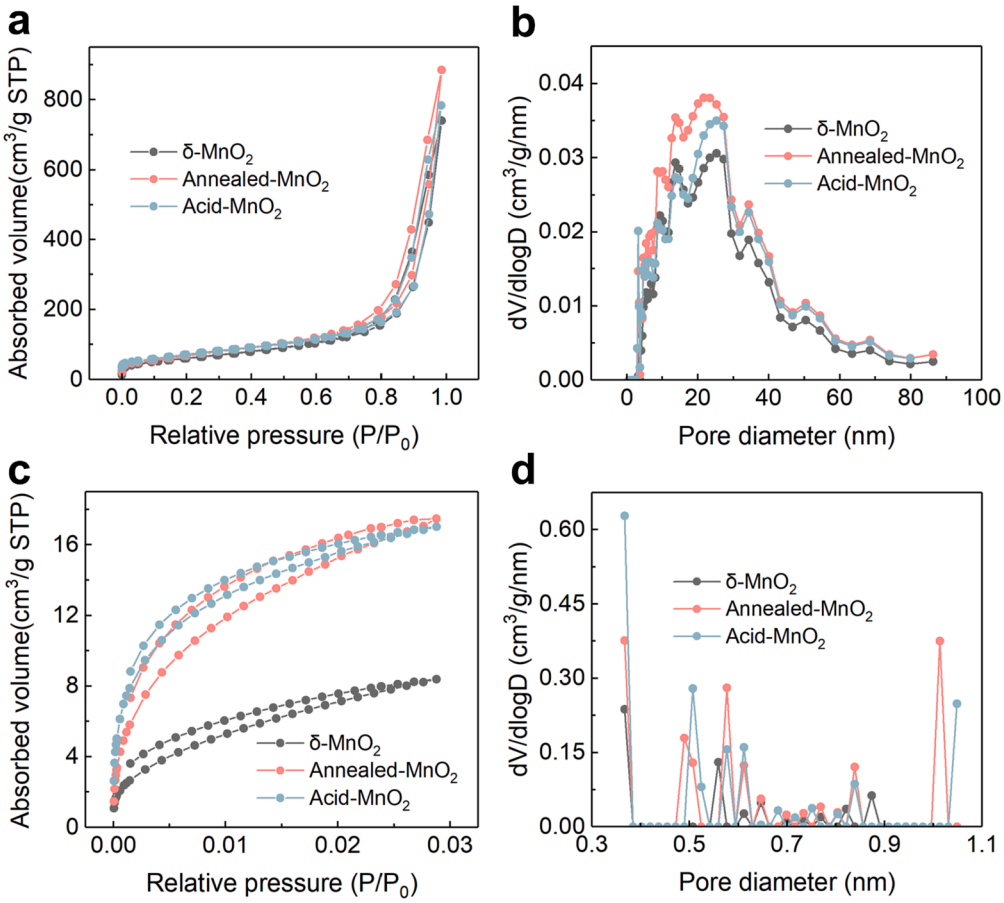

Fig. 3. Gas sorption isotherms for the characterization of δ-MnO_2 catalysts: (a) N_2 adsorption–desorption test (77 K) and (b) corresponding pore size distributions of δ-MnO_2, annealed-MnO_2, and acid-MnO_2. (c) CO_2 adsorption–desorption test (273 K) and (d) the resulting pore size distributions of the catalysts.

Table 2
Morphological parameters of δ-MnO_2, annealed-MnO_2, and acid-MnO_2.

Catalyst	S_{BET} (m^2/g)[a]	S_{DFT} (m^2/g, 0.35–1.05 nm)[b]	S_{DFT} (m^2/g, 0.35–0.70 nm)
δ-MnO_2	245.2	41.1	35.4
Annealed-MnO_2	279.0	108.4	77.1
Acid-MnO_2	265.2	120.7	105.2

[a] S_{BET} represents the specific surface area calculated by N_2-BET (Brunauer-Emmett-Teller) model. Note that the S_{BET} of δ-MnO_2 catalysts synthesized in this work are much higher than δ-MnO_2 prepared *via* traditional hydrothermal methods (30 to 130 m^2/g, [7,8,12,15,41]).

[b] S_{DFT} represents the specific surface area calculated by CO_2-DFT (Density Functional Theory) model.

within the δ-MnO_2 interlayers and the exposure of interlayer spaces, corroborated with our findings of Na^+ ion and water removal.

In the case of annealing, the dehydration process can be attributed directly to the removal of structural water and partial dehydrogenation of the hydrate cations at 200 °C. For acid-MnO_2, the expelling of Na ions from the lattice space during the acid treatment enabled a more efficient and thorough dehydration process. The water present within the inter-lamellar space was nearly entirely removed during the subsequent drying at 150 °C. This aligns with a previous study, which suggested that water within the inter-layered structure of δ-MnO_2 could be removed as low as 132 °C [42]. In this way, the expulsion of Na^+ ions and the removal of H_2O effectively cleared the blockage in the interlayer space of the δ-MnO_2, allowing the previously enclosed sub-nanometer inter-layer spaces and inner active sites to be exposed to reactant molecules. While some studies suggest that alkali ions and water crystals act as stabilizing pillars within the interlayer regions of layered materials [43], it is more likely that the underlying causes of layer breakages can be attributed to the external forces exerted on δ-MnO_2 during the removal of ions and water, rather than solely the absence of these components [44]. This is supported by the observation of a relaxed confinement effect in the vertical direction between the layers, as evidenced by Raman spectroscopy (Fig. 2b). The HRTEM and XRD results (Fig. 1 and Fig. 2a) strongly support the stability of the layers after removal of H_2O and Na^+ ions, which agrees with the work of Kim et al., who demonstrated that δ-MnO_2 could maintain its layered structure and interlayer spacing unchanged even after dehydration as high as even 300 °C [42].

The removal of interlayer obstructions in δ-MnO_2 can significantly change the acidity of the catalysts. Fig. 4a presents the thermal desorption profiles of δ-MnO_2 samples previously saturated with NH_3. Notably, both annealed-MnO_2 and acid-MnO_2 exhibit much more pronounced ammonia desorption intensities compared to δ-MnO_2, indicating a higher number of acid sites. Zheng et al. reported that the evolution of NH_3 below 300 °C and between 300 °C and 600 °C can be attributed to the presence of weak and moderate acid sites on the δ-MnO_2 samples, respectively [14]. Therefore, we believe that annealing and acid treatments significantly increased both weak and moderate acid sites on δ-MnO_2. (We refrained from conducting NH_3-TPD test at higher temperatures due to the transformation of δ-MnO_2 materials into α-MnO_2 at approximately 500 °C [7]). Since we have confirmed the removal of interlayer blockages (interlayer structural water and sodium-ion hydrates) without altering the morphology and lattice structure of annealed-MnO_2 and acid-MnO_2 catalysts, the substantial increase in acid sites can be attributed to the exposure of 2D sub-nanometer spaces and the interlayered acid sites to NH_3 molecules. When the interlayer

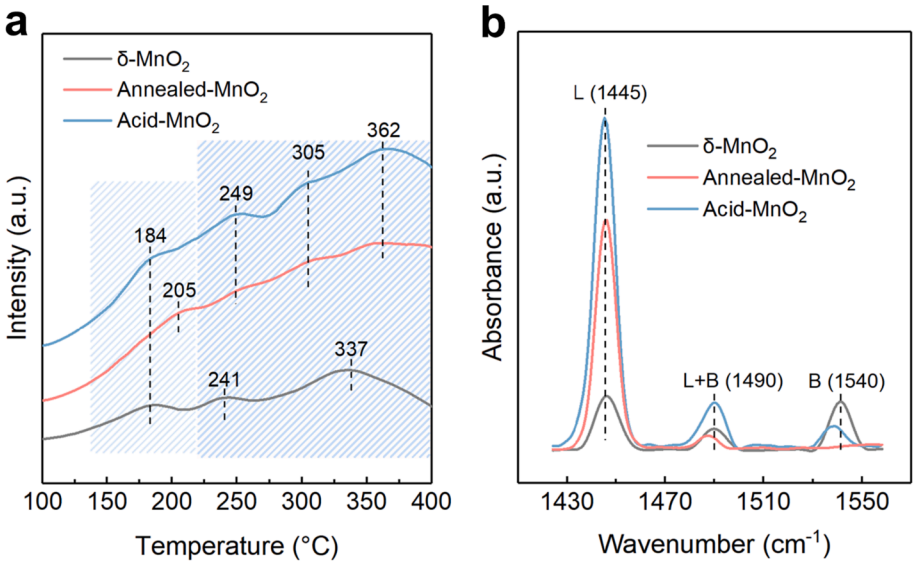

Fig. 4. Clearing the inter-lamellar space aids in exposing Lewis-acid sites confirmed by NH_3-TPD and Pyridine-IR spectra. (a) NH_3-TPD profiles and (b) Pyridine-IR spectra of δ-MnO_2, annealed-MnO_2, and acid-MnO_2.

obstructions were removed, molecules with smaller dimensions than the interlayer gaps (e.g., NH_3, 2.6 Å) could enter the interlayer and adsorb on the acid sites in the interlayered space, subsequently desorbing during the temperature ramp-up process and resulting in a significantly increased NH_3 intensity. Alongside the increased NH_3 intensity, we also noted that the NH_3 desorption peak positions for annealed-MnO_2 and acid-MnO_2 deviate from those of pristine δ-MnO_2 (except peaks at 184 °C). This finding suggests that the NH_3 desorbed from annealed-MnO_2 and acid-MnO_2 originate from different locations compared to that from pristine δ-MnO_2: the interlayers and surfaces of the samples, respectively.

The Py-IR spectra provided a more comprehensive insight, revealing that the substantial increase in acid sites primarily resulted from the expansion of Lewis-acid sites. According to the literature, the peak at 1450 cm^{-1} is attributed to pyridine adsorbed on Lewis-acid sites; the band at 1540 cm^{-1} is associated with pyridine adsorbed on Brønsted-acid sites; the band at 1490 cm^{-1} can be assigned to pyridine adsorbed on both Lewis-acid sites and Brønsted-acid sites [45]. As shown in Fig. 4b, the modified δ-MnO_2 catalysts exhibit a notable increase in Py-IR intensity, signifying a substantially higher number of Lewis-acid sites for pyridine adsorption on acid-MnO_2 and annealed-MnO_2 compared to pristine δ-MnO_2. The content of Lewis-acid sites on acid-MnO_2 and annealed-MnO_2 was estimated to be 0.127 mmol/g and 0.083 mmol/g, respectively, significantly higher than that of the pristine δ-MnO_2 (0.034 mmol/g), as calculated by the integrated absorbance of the Lewis-acid site bands at 1445 cm^{-1} [46]. Considering that no obvious changes were observed in the morphology, surface area, and lattice structure of δ-MnO_2 after annealing or acid treatment, the additional approximately 0.09 and 0.05 mmol/g Lewis-acid sites identified in acid-MnO_2 and annealed-MnO_2, respectively, compared to the pristine δ-MnO_2, are likely due to the newly exposed internal Lewis-acid sites situated within the inter-lamellar space of the δ-MnO_2 following the cleaning of the interlayers. Fig. 5 illustrates the scheme of pyridine adsorption on δ-MnO_2, annealed-MnO_2, and acid-MnO_2. When the interlayer gaps of δ-MnO_2 are occupied by interlayer structural water and sodium ion hydrates, pyridine molecules are restricted to adsorbing onto the surface Lewis-acid sites of δ-MnO_2. However, after the removal of these internal obstructions, pyridine could not only adsorb onto the surface of the δ-MnO_2 nanosheets, but also diffuse into the sub-nanometer crystal lattice layers under the concentration gradient and adsorb onto the interlayer Lewis-acid sites. Similarly, when the catalysts with unobstructed interlayers are used in toluene ozonation, toluene may also enter the interlayers and be adsorbed on the inner Lewis-acid sites. In addition, both acid treatment and annealing treatment decreased the intensity of Brønsted-acid sites, which could be attributed to the loss of hydroxyl groups within the interlayer space and on the surface [47]. This result thus excludes the impact of Brønsted-acid sites as a potential variable on catalyst activity.

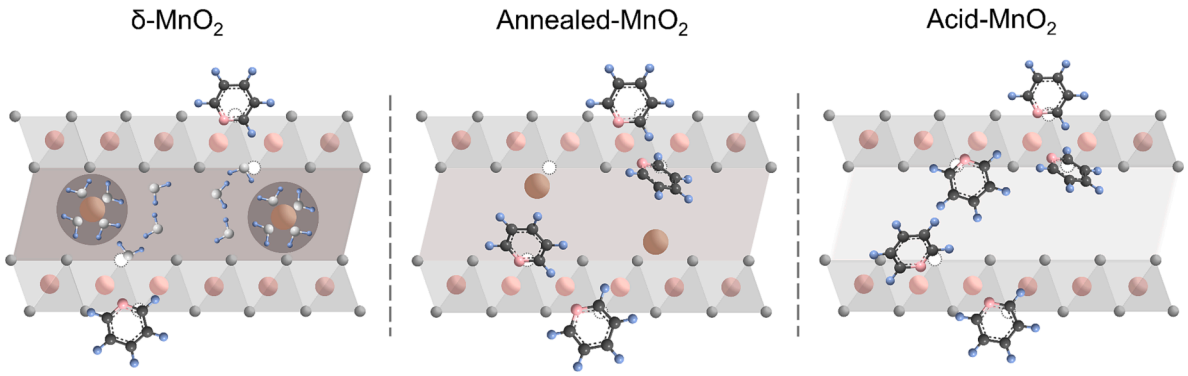

Fig. 5. Schematic illustration of pyridine adsorption on δ-MnO_2, annealed-MnO_2, and acid-MnO_2, highlighting that following thermal annealing and acid treatment, the interlamellar space of δ-MnO_2 become readily accessible for pyridine molecules, allowing them to enter and adsorb onto the Lewis-acid sites situated within the interlamellar space.

Therefore, the characterization of the δ-MnO_2 catalysts confirms that the acid and annealing treatments primary cleared the interlayers and effectively exposed the Lewis-acid sites in the confined space without changing the physicochemical properties (including crystal phase, structures, and the content of the oxygen vacancy) of the catalysts, thus excluding any change in catalytic activity caused by the aforementioned factors.

3.2. Catalytic performance

To demonstrate the basic activity of the δ-MnO_2 catalysts on ozone conversion, ozone was generated by the DBD reactor and converted by the various catalysts (i.e., δ-MnO_2, acid-MnO_2, annealed-MnO_2, and cap-MnO_2). As shown in Fig. 6a and b, increasing the SIE from 131 to 288 J/L significantly enhanced the ozone concentration generated by plasma discharge from ~120 to ~1000 ppm, regardless of the presence of toluene, indicating that the presence of trace concentration toluene would not interfere with ozone generation. All catalysts demonstrated high and comparable ozone conversion activity, which can be attributed not only to an abundance of oxygen vacancies to promote ozone conversion, but also to the interlayers of each catalyst, which can provide free access to ozone molecules. Since pyridine molecules are allowed to enter the clear sub-nanometer space (i.e., the interlayer space of acid-MnO_2 and annealed-MnO_2), ozone molecules with a smaller dynamic scale should be permitted as well. As δ-MnO_2 and cap-MnO_2 performed similarly to acid-MnO_2 and annealed-MnO_2, it can be concluded that interlayers with obstacles (structural water and hydrated cations) could also allow free access to ozone molecules. As evidenced by Py-IR, the available Lewis-acid sites on acid-MnO_2 and annealed-MnO_2 are far more abundant than those on δ-MnO_2. Meanwhile, the Lewis-acid sites of cap-MnO_2 are deactivated. However, such large changes in Lewis-acid sites had no effect on the ability of the catalysts to convert ozone, suggesting that Lewis-acid sites are unrelated to the ozone conversion process. In other words, acidification of δ-MnO_2 neither enhances nor suppresses the production of active oxygen radicals. Moreover, the introduction of toluene has little effect on the catalytic activity for ozone conversion, implying that toluene has a distinct adsorption site, and thus the adsorption of toluene on the catalysts will not interfere with the ozone conversion on oxygen vacancies.

The conversion of toluene as a function of SIE from 131 to 288 J/L in the two-stage plasma catalysis system was carried out, and the corresponding reaction performance is shown in Fig. 6c. According to our previous work, the decomposition of toluene in plasma is mainly attributed to the reactions initiated by electrons and active species (e.g., OH, H and O radicals) [6]. Herein, in the first-stage NTP-alone process, toluene conversion increased from 19.2% to 73.1% when increasing the SIE from 133 J/L to 288 J/L. In this process, only a portion of toluene was converted with the formation of a large amount of ozone, which will serve as an oxidant for toluene oxidation in the subsequent catalytic step. The coupling of NTP with a catalytic process largely increased the conversion of toluene, indicating the importance of ozonation of toluene over the δ-MnO_2 catalysts. Among the different catalysts, acid-MnO_2 and annealed-MnO_2 exhibited significantly improved catalytic activity for toluene oxidation. Compared to δ-MnO_2 (30.5%–96.7%), both acid-MnO_2 and annealed-MnO_2 showed higher toluene conversion, reaching 41.8%–100% and 40.3%–99.2%, respectively. In addition, the acid-MnO_2 showed an energy yield of 14.0–11.8 g kWh^{-1} at an SIE range of 170–288 J/L, which demonstrated the best performance compared to previous works on plasma-catalytic toluene conversion (Fig. S5) [6,48–55]. By contrast, cap-MnO_2 showed weak catalytic activity and contributed less toluene conversion than the pristine δ-MnO_2. Specifically, the contribution of the catalysts alone to toluene conversion was compared at an SIE of 170 J/L. Under this condition, the NTP converted 39.8% of the toluene and generated 377 ppm ozone. In a catalytic reactor, the δ-MnO_2 with the 377 ppm ozone contributed to around 10% of toluene conversion, bring the total conversion to 49.8%. In this way, toluene conversion by acid-MnO_2, annealed-MnO_2 and cap-MnO_2 with the same concentration of ozone was calculated to be 30.2%, 21.8% and 3%, respectively. Considering the conversion of toluene by catalytic oxidation, the catalyst activity was increased by 2 and 1.2 times after the

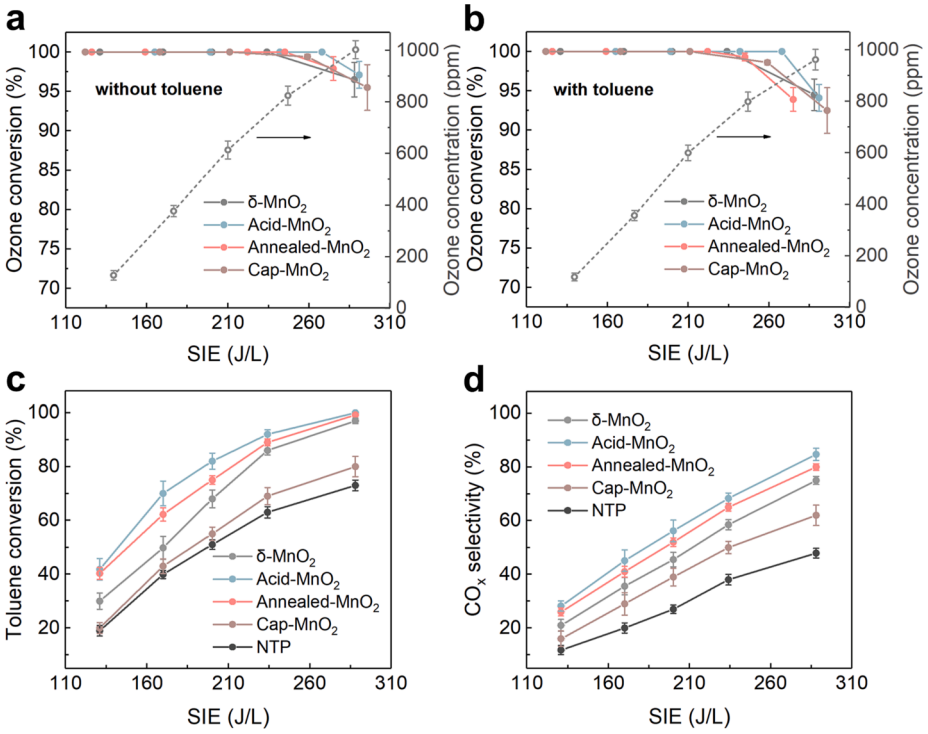

Fig. 6. Performance of the two-stage plasma system using different δ-MnO_2 catalysts for ozone and toluene conversion. (a, b) Ozone concentration and conversion without and with toluene introducing. (c) Toluene conversion and (d) CO_x selectivity in NTP and plasma-catalytic processes. Reaction conditions: 0.2 g catalyst, toluene concentration = 230 ppm, total gas flow rate = 0.5 L/min.

acid and annealing treatments, respectively, and decreased by 70% when Lewis-acid sites were capped by pyridine molecules. The CO_x selectivity, which represents the oxidation degree of toluene, followed the same pattern. When compared to pristine δ-MnO_2, acid-MnO_2 and annealed-MnO_2 showed higher CO_x selectivity (Fig. 6d), most likely due to the much-promoted mass transfer and oxidation of toluene and its intermediates.

Considering that VOCs are often emitted in humid environments, we further investigated the plasma-catalytic oxidation of toluene under varying humidity conditions (Fig. S6). At ambient temperature (25 °C) and under relative humidity levels ≤ 50%, water vapor notably enhanced toluene conversion using NTP alone, which can be attributed to the generation of active radicals like O and OH through plasma dissociation of H_2O. However, higher humidity levels had an adverse effect on toluene conversion due to the quenching of plasma species by excess water vapor. The introduction of water vapor resulted in decreased toluene conversion and CO_x selectivity in the plasma-catalytic process. This deactivation effect was particularly pronounced for the acid-MnO_2 and annealed-MnO_2 catalysts. Notably, at 100% humidity, the differences between the catalytic performance of acid-MnO_2, annealed-MnO_2, and δ-MnO_2 became negligible. These findings suggest that the additional Lewis-acid sites in acid-MnO_2 and annealed-MnO_2 catalysts are more susceptible to deactivation by water molecules.

Since other catalytic characteristics of the catalysts (e.g., crystal phase, specific surface area, pore size distribution, and oxygen vacancies) that would affect catalytic activities have been demonstrated to remain nearly unchanged, the improved oxidation of toluene with acid-MnO_2 and annealed-MnO_2 can be attributed to significantly increased available Lewis-acid sites. As proved before, acid and annealing treatments can greatly remove H_2O and/or Na cations from the δ-MnO_2 interlayers, potentially exposing internal space with Lewis-acid sites to the reactant molecules. To confirm this hypothesis, we evaluated the adsorption capacity of these catalysts for toluene using an adsorption-penetration measurement [56], where the removal of toluene was only due to adsorption of toluene by the catalysts. As presented in Fig. 7, the first breakthrough times (t_b, at C/C_0 = 0.05) of acid-MnO_2 and annealed-MnO_2 were 39.6 min and 33.8 min, respectively, which were longer compared to δ-MnO_2 (26.9 min). The cap-MnO_2 showed the shortest t_b (15.9 min), which can be attributed to the occupation of the surface sites by pyridine molecules and the already closed internal space. In addition, the toluene adsorption capacity of the δ-MnO_2 samples follows the order: acid-MnO_2 (1.273 mmol/g) > annealed-MnO_2 (1.153 mmol/g) > δ-MnO_2 0.969 mmol/g) > cap-MnO_2 (0.632 mmol/g), which is in good agreement with the concentration of Lewis-acid sites. This finding implies that the catalyst with more available Lewis-acid sites is more favorable for toluene absorption. According to the L-H mechanism, the two reactant molecules must be adsorbed on adjacent active sites on the catalyst surface for the reaction to occur. In this experiment, specifically in the catalytic toluene ozonation stage, oxygen vacancies served as active sites for ozone. Notably, the quantities of these vacancies remained constant across various catalysts, resulting in comparable ozone conversion. However, the increased number of Lewis-acid sites directly correlated with significant improvements in both the adsorption and conversion of toluene. This finding demonstrates that Lewis-acid sites play an equally important role as oxygen vacancies in the catalytic ozonation of toluene over δ-MnO_2. However, the indispensable role of Lewis-acid sites has been largely overlooked, substantially compromising the catalytic performance.

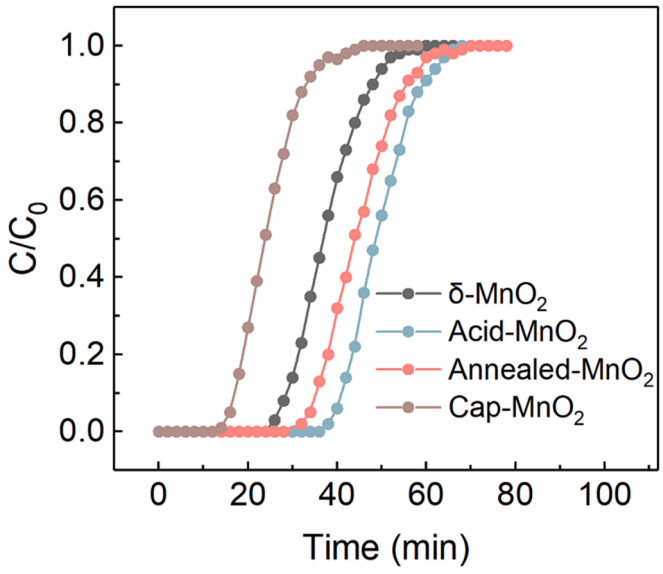

Fig. 7. Toluene adsorption penetration curves of the as-synthesized δ-MnO_2, acid-MnO_2, annealed-MnO_2, and cap-MnO_2 samples in dry air (without O_3). The adsorption conditions: 0.2 g catalyst, toluene concentration = 230 ppm, total gas flow rate = 0.5 L/min. C and C_0 represent the concentration of toluene after and before the packed-bed reactor. Note that the toluene concentration was measured using Gasmet rather than GC, for rapid data collection.

In the two-stage plasma catalysis system, reaction intermediates or byproducts (e.g., benzaldehyde, benzoic acid, phenol, benzene and nitrobenzene) could form in the first NTP stage and then be carried over to the second catalytic stage [6], potentially affecting the precise analysis of toluene conversion during the catalytic ozonation step. Therefore, we further performed one-step catalytic ozonation of toluene, using the DBD reactor solely as an ozone generator to ensure that the conversion of toluene occurred entirely through ozone-assisted oxidation over the catalysts. Fig. 8a presents the effect of the δ-MnO_2, acid-MnO_2, annealed-MnO_2, and cap-MnO_2 catalysts on the conversion of toluene as a function of ozone concentration. In general, the toluene conversion of each catalyst increased with increasing ozone concentration. Similar to the plasma catalysis case, the catalyst with a higher content of Lewis-acid sites converted toluene more efficiently. Since all these catalysts can completely decompose the inlet ozone (Fig. S7), this suggests that an equivalent quantity of active oxygen species was generated under the same ozone concentrations. Therefore, a catalyst with a greater number of available Lewis-acid sites would undoubtedly be able to use these ozone-converted active oxygen species more effectively, resulting in a higher rate of toluene conversion.

Table 3 summarizes the concentrations of Lewis-acid sites in different catalysts (i.e., δ-MnO_2, acid-MnO_2 and annealed-MnO_2) as well as the initial reaction rates of toluene (r_{Tol}) at different ozone/toluene ratios (i.e., 0.6, 1.3, and 2.0). We correlated the values of r_{Tol} with the concentration of Lewis-acid sites. Note that the performance of cap-MnO_2 is not included in Table 3 as it is difficult to estimate the concentration of available Lewis-acid sites after the pyridine capping. As illustrated in Fig. 8c, a positive linear relationship exists between the Lewis-acid site presents and the r_{Tol} with correlation coefficient (R^2) at 0.99, suggesting that the Lewis-acid sites contributes significantly to the performance of δ-MnO_2 for catalytic toluene ozonation.

Therefore, a novel and integrated ozone-assisted catalytic toluene oxidation scenario in sub-nanometer confined space of the δ-MnO_2 catalysts is proposed: Molecules with relatively smaller kinetic diameters such as ozone can diffuse into the inter-lamellar space under the gradient of concentration through the nanosheet framework, regardless of presence of structural water or hydrated cations within the interlayers. Hence, all the δ-MnO_2 catalysts (i.e., δ-MnO_2, acid-MnO_2, annealed-MnO_2, and cap-MnO_2) can effectively convert ozone over their inner and external oxygen vacancies, which is evident from the same ozone conversion capacitance among the catalysts. However, the conversion of ozone does not always contribute to toluene oxidation. When ozone diffuses into the confined space with obstacles (i.e., interlayer space of the pristine δ-MnO_2), it is converted into O_2 (ref. [4]) while toluene and other by-products or reaction intermediates are left outside the interlayer channels [8]. Therefore, although the pristine δ-MnO_2 can

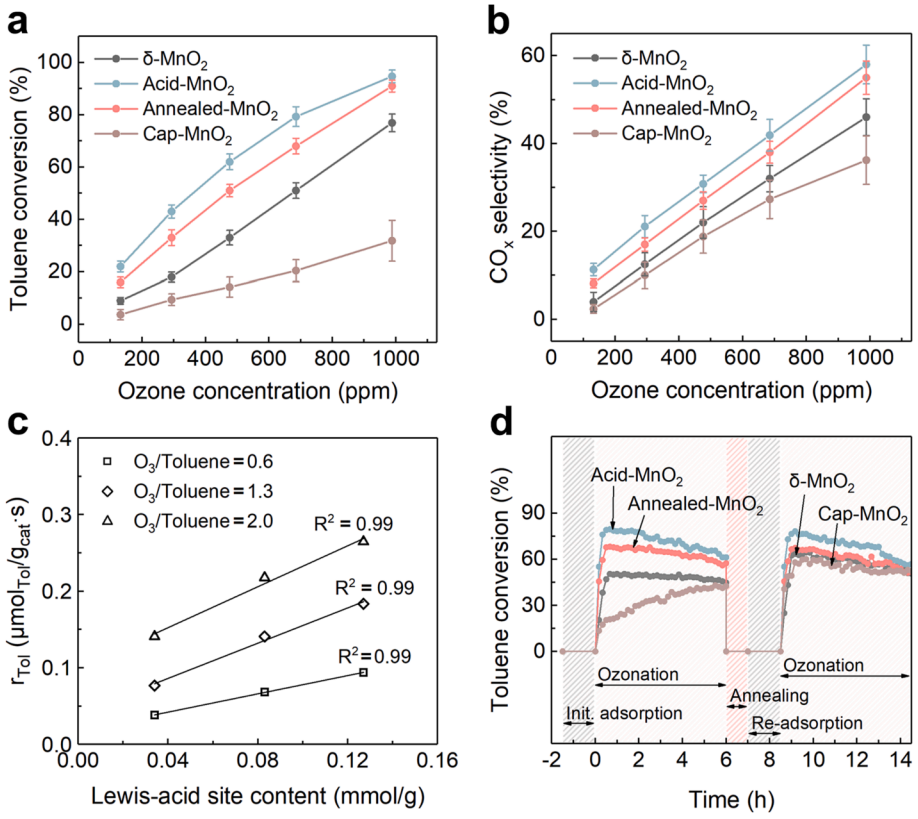

Fig. 8. One-step catalytic ozonation of toluene without plasma decomposition. (a) Toluene conversion and (b) CO_x selectivity as a function of ozone concentration. (c) Dependences of the initial reaction rates of toluene (r_{Tol}) on the values of Lewis-acid sites in different O_3/toluene ratios (based on the data in the ozonation experiment). (d) Toluene conversion as a function of time during 5 sequential steps (i.e., 1.5-h toluene adsorption/saturation, 6-h catalytic toluene ozonation, 1-h catalyst regeneration, 1.5-h toluene adsorption/saturation, and another 6-h catalytic toluene ozonation). Reaction conditions: 0.2 g catalyst, toluene concentration = 230 ppm, total gas flow rate = 0.5 L/min.

Table 3
Experimental data of the one-stage catalytic toluene ozonation.

Catalyst	L-site content (mmol/g)	Initial reaction rates of toluene ($\mu mol_{Tol}/g_{cat}·s$)		
		O_3/Tol = 0.6	O_3/Tol = 1.3	O_3/Tol = 2.0
δ-MnO_2	0.034	0.0384	0.0769	0.1409
Annealed-MnO_2	0.083	0.0683	0.1409	0.2178
Acid-MnO_2	0.127	0.0939	0.1836	0.2647

also achieve high and comparable ozone conversion, a significant portion of the ozone does not participate in the oxidation reactions throughout. However, when the hydrated Na cations and structural H_2O contained within the inter-lamellar space are removed (i.e., interlayer space of acid-MnO_2 and annealed-MnO_2), toluene can diffuse into the interlayers and be adsorbed on the internal Lewis-acid sites, ready to be oxidized by ozone converted active oxygen species (e.g., O_2^{2-}) [11]. One might claim that the enhanced catalytic activity towards toluene conversion over acid-MnO_2 and annealed-MnO_2 is only due to the enlarged contact area that results from the exposure of interlayer space, where toluene can be catalytically oxidized by ozone solely without the participation of the Lewis-acid sites. However, if this were the case, cap-MnO_2 would have similar performance to pristine δ-MnO_2, as both of them possess comparable oxygen vacancies for ozone conversion and they both only allow ozonation reactions on their surface. Contrarily, cap-MnO_2 with deactivated Lewis-acid sites showed significantly lower toluene conversion, revealing the importance of the Lewis-acid sites on the reverse side.

The stability of the catalysts during catalytic ozonation was further investigated at an ozone concentration of 685 ppm (Fig. 8d). During a six-hour test, the toluene conversion of δ-MnO_2 decreased slightly from 50.4% to 44.8%. Although the toluene conversion of acid-MnO_2 (79.6%) and annealed-MnO_2 (68.3%) was much higher in the initial stage than that of pristine δ-MnO_2, it dropped much faster. After six hours of reaction, the toluene conversion of acid-MnO_2 and annealed-MnO_2 decreased by 21.3% to 62.6% and 16.7% to 56.9%, respectively. By contrast, only an 11.1% decrease was observed with δ-MnO_2. The faster deactivation of acid-MnO_2 and annealed-MnO_2 can be explained by the re-blockage of the inter-lamellar space caused by H_2O accumulation during toluene oxidation. Unlike pristine δ-MnO_2, acid-MnO_2 and annealed-MnO_2 allow oxidation to occur in the confined inter-lamellar space. Naturally, ozonation of toluene and its intermediates resulted in the formation and accumulation of water molecules in the confined space. As internal chemisorbed water accumulated, toluene was refused entry into the interlayer space. This process explained the catalysts with unblocked inter-lamellar space deactivated more quickly. As shown in Fig. S8a, compared to fresh acid-MnO_2, spent catalysts had a significantly higher O_{H2O} peak in the XPS O 1s spectra after 6 and 12 h of toluene ozonation reaction. Meanwhile, the Mn^{3+}/Mn^{4+} and O_{surf}/O_{latt} ratios remained almost unchanged (Fig. S8b), ruling out catalyst deactivation due to the gradual vanishing of oxygen vacancies. Notably, the toluene conversion of cap-MnO_2 increased with reaction time, potentially due to the gradual consumption of pyridine molecules and the subsequent re-exposure of the capped Lewis-acid sites. After annealing the spent catalysts in an Ar atmosphere at 200 °C for two hours, the catalytic activity of the H_2O-sweeped δ-MnO_2 catalysts was recovered, and the δ-MnO_2 and cap-MnO_2 even exhibited higher activity than their initial activity. These findings further confirm that cleaning the blockage

and exposing the Lewis-acid sites in the interlayered space of δ-MnO_2 ensures the high catalytic activity for toluene oxidation.

3.3. Reaction mechanisms

Cleaning the interlayers and exposing Lewis-acid sites in the interlamellar space improved not only the initial decomposition of toluene but also its complete oxidation. In the two-stage plasma-catalytic toluene conversion and single-step catalytic toluene ozonation, both acid-MnO_2 and annealed-MnO_2 showed higher CO_x selectivity. This finding can be attributed to the greatly enhanced oxidation of intermediates other than toluene as a result of the opening of the interlayered space and improved ozone utilization. In addition to toluene, incomplete oxidation products such as benzaldehyde, benzoic acid, and benzene, can also enter the interlayer and be oxidized. Moreover, we found that δ-MnO_2 with rich Lewis-acid sites can further promote the oxidation of intermediate products with specific functional groups. As revealed by GC-MS analysis (Fig. 9), the proportion of esters, hydrazides, and ketones in the byproducts decreased significantly as the number of Lewis-acid sites increased, indicating accelerated decomposition of these species. This finding is consistent with previous research that reported Lewis-acid sites could promote their adsorption and conversion [57–61]. Meanwhile, more Lewis-acid sites produced more alcohols and aldehydes, which can be explained by accumulation in dynamic processes in which the formation of these intermediates exceeds their decomposition, resulting in an increase in the concentration

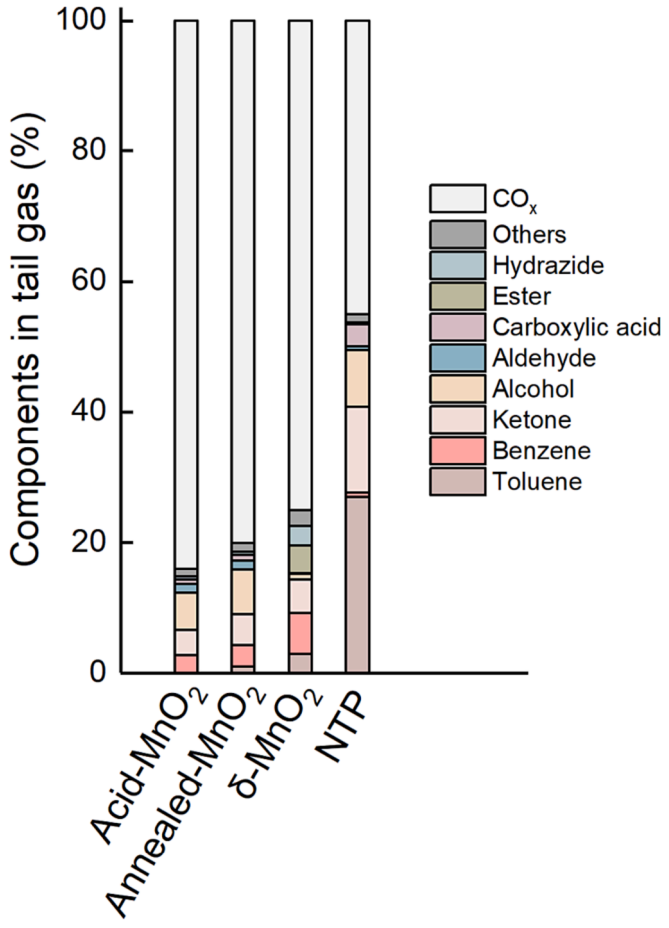

Fig. 9. Byproducts analysis of toluene decomposition in NTP and two-stage plasma catalysis processes. The byproducts were classified into function groups and calculated semi-quantitatively using area normalization based on GC-MS analysis. Reaction conditions: 0.2 g catalyst, toluene concentration = 230 ppm, total gas flow rate = 0.5 L/min, SIE = 288 J/L.

of these intermediates. Other products, including ethers, alkanes, furans, and nitro organics, were also detected in the exhausted gas. Table S1 shows the specific composition of the effluents. Notably, the formation of hydrazides and nitro compounds can be attributed to the ammoniation and nitration of hydrocarbons with plasma-induced nitrogen-containing species (e.g., NO_x and NH_x). While NO_x contributes to the conversion of toluene, it can be hazardous if released into the atmosphere. Hence, the concentrations of NO_x (including NO, NO_2, and N_2O) generated by NTP alone and remained after the plasma-catalytic process (acid-MnO_2 catalyst) were measured (Fig. S9). The NO_x concentration generated in our experiment were similar to previously reported values [62].

A plausible degradation pathway of toluene and some essential contributing reactions in the plasma-catalytic process is illustrated in Fig. 10 based on the partially oxidized intermediates detected by GC-MS and our previous work [6,63]. In the first stage NTP process, critical reactions can be divided into two categories: ozone generation and partial oxidation of toluene. The generation of ozone by NTP is critical for the complete oxidation of toluene and reaction intermediates in the following catalytic stage. In the DBD reactor, oxygen molecules split into atomic oxygen through electron impact dissociation. Then, atomic oxygen will react with oxygen molecules in the presence of a third body (e.g., O_2, N_2 or the reactor wall) to produce ozone [64]. In the electron impact dissociation of toluene, the relatively weak C-H bonds and C-C bonds connecting benzene and methyl are prone to breaking first, resulting in the formation of benzyl, phenyl, and methyl radicals [6,65,66]. Moreover, the electron impact dissociation of toluene and its fragments produces hydrogen atoms, which react with O and N atoms to form OH, NH_x, NO_x, etc. These polyatomic groups, together with the active monoatomic species (i.e., O, N, and H) and electrons, contribute to the continued conversion of toluene and reaction intermediates. During the conversion of toluene and its fragments via plasma-induced active species, various functional groups, including hydroxyl, carbonyl, carboxyl, nitro and amino, are grafted on hydrocarbon fragments. When the gas flow exits the DBD reactor, a small portion of toluene is converted to CO_x, but the majority of the carbon remains organic and toxic.

The adsorption and catalytic ozonation of unconverted toluene and reaction intermediates in the second-stage catalytic process are critical to achieving a high mineralization level of toluene. Specifically, the ozone-assisted oxidation over the best-performing acid-MnO_2 includes two main reactions: catalytic ozone conversion and subsequent catalytic oxidation of toluene and reaction intermediates. Acid-MnO_2, like ordinary layered δ-MnO_2 catalysts, allows ozone to access both of its surface and interlayered oxygen vacancies, resulting in effective conversion of ozone to active oxygen species (e.g., O_2^{2-}) for the subsequent catalytic oxidation [4]. More importantly, the removal of hydrated cations and structural water in inter-lamellar space of the δ-MnO_2 catalyst by acid washing and subsequent drying allow toluene and other intermediates with relatively large kinetic diameters (e.g., benzaldehyde, benzene, and acetic acid ethenyl ester) diffuse into the inter-lamellar space instead of only stay at the catalyst surface, being adsorbed on the internal Lewis-acid sites and oxidized by the ozone-converted active oxygen species. As a result, combining plasma with the inter-lamellar space unblocked δ-MnO_2 catalyst significantly enhances the oxidation of toluene while reducing the formation of organic byproducts.

4. Conclusion

The most efficient method to enhance the catalytic activity of a catalyst in a particular reaction is to identify and increase the exact active sites. However, this has not been achieved effectively in the catalytic oxidation of toluene using δ-MnO_2 catalysts. Herein, we report a facile displacement method to synthesize δ-MnO_2 with a complete layered structure and a large specific surface area. By annealing and nitric acid treatment, the hydrated cations and structural water in inter-lamellar space of the δ-MnO_2 sample were removed. As a result, the

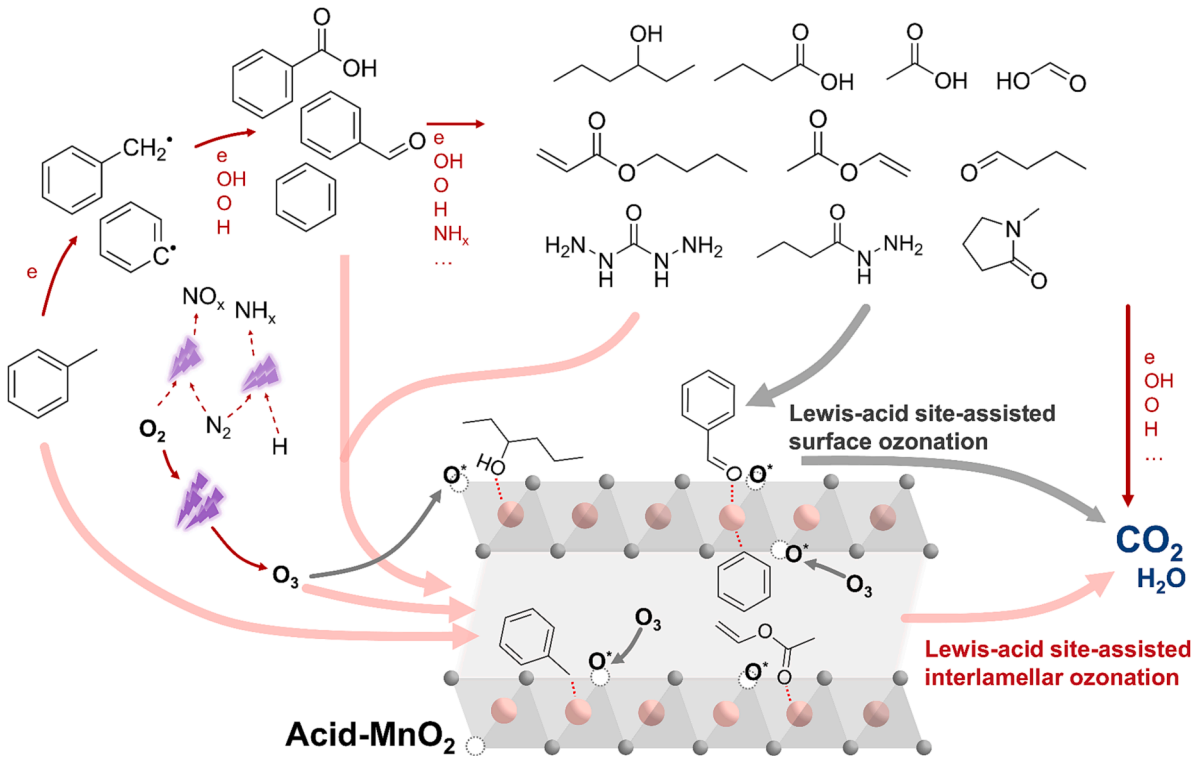

Fig. 10. Possible reaction pathways of toluene conversion in the two-stage plasma catalysis process. Toluene is initially decomposed by plasma and then catalytic ozonated over acid-MnO_2 both on the outer surface and within the layered structure. The interlamellar ozonation, assisted by the internal Lewis-acid sites, significantly enhances the efficient utilization of ozone-derived active oxygen species, leading to the complete oxidation of toluene.

internal Lewis-acid sites became naturally accessible to molecules which were previously forbidden. The "interlayer-cleaned" δ-MnO_2 with freely accessible Lewis-acid sites exhibited superior toluene adsorption and conversion performance compared to the interlayer-blocked δ-MnO_2. Conversely, the catalyst with deactivated Lewis-acid sites showed poor toluene conversion. The correlation analysis between the Lewis-acid sites and the reaction rate of toluene conclusively indicates that the Lewis-acid sites are the catalytically active sites for toluene activation. This confirms that the heterogeneous reaction between toluene and ozone follows the L-H mechanism. Moreover, GC-MS analysis revealed that Lewis-acid site-rich δ-MnO_2 can further promote the oxidation of some intermediates with specific functional groups, contributing to the more complete oxidation of toluene. This work presents a promising strategy for the synthesis of highly efficient δ-MnO_2 catalysts for plasma (ozone)-assisted catalytic oxidation of VOCs. It also provides valuable insights into the modulation of potential active sites and the rational design and optimization of the catalysts, which are important for the field of environmental catalysis.

CRediT authorship contribution statement

Zheng Bo: Conceptualization, Funding acquisition, Project administration, Supervision, Writing – review & editing, Resources. **Mengyu Cao:** Conceptualization, Data curation, Formal analysis, Investigation, Methodology, Visualization, Writing – original draft, Writing – review & editing. **Huihui Zhang:** Formal analysis. **Yaolin Wang:** Formal analysis, Investigation, Supervision, Writing – review & editing. **Jianhua Yan:** Conceptualization, Funding acquisition, Project administration, Supervision, Writing – review & editing. **Kefa Cen:** Resources, Writing – review & editing. **Kostya (Ken) Ostrikov:** Conceptualization, Supervision, Writing – review & editing. **Xin Tu:** Conceptualization, Funding acquisition, Project administration, Supervision, Writing – review & editing.

Declaration of competing interest

The authors declare that they have no known competing financial interests or personal relationships that could have appeared to influence the work reported in this paper.

Data availability

Data will be made available on request.

Acknowledgements

We gratefully acknowledge the funding support from the National Natural Science Foundation of China (No. 52076188), the Royal Society Newton Advanced Fellowship (No. 52061130218), and the Engineering and Physical Sciences Research Council (EP/V036696).

Appendix A. Supplementary data

Supplementary data to this article can be found online at https://doi.org/10.1016/j.cej.2023.148399.

References

[1] X. Liang, X. Sun, J. Xu, D. Ye, Improved emissions inventory and VOCs speciation for industrial OFP estimation in China, Sci. Total Environ. 745 (2020) 140838–140849.
[2] Z. Zhang, F. Lin, L. Xiang, H. Yu, Z. Wang, B. Yan, G. Chen, Synergistic effect for simultaneously catalytic ozonation of chlorobenzene and NO over $MnCoO_x$ catalysts: Byproducts formation under practical conditions, Chem. Eng. J. 427 (2022) 130929–130943.
[3] Y. Zhang, M. Wu, Y. Wang, Y.H. Kwok, W. Pan, W. Szeto, H. Huang, D.Y.C. Leung, Fluorinated TiO_2 coupling with α-MnO_2 nanowires supported on different substrates for photocatalytic VOCs abatement under vacuum ultraviolet irradiation, Appl. Catal. B: Environ. 280 (2021) 119388–199399.
[4] R. Yang, Z. Guo, L. Cai, R. Zhu, Y. Fan, Y. Zhang, P. Han, W. Zhang, X. Zhu, Q. Zhao, Z. Zhu, C.K. Chan, Z. Zeng, Investigation into the phase-activity

relationship of MnO_2 nanomaterials toward ozone-assisted catalytic oxidation of toluene, Small. 17 (2021) 2103052–2103062.
[5] A. Bogaerts, X. Tu, J.C. Whitehead, G. Centi, L. Lefferts, O. Guaitella, F. Azzolina-Jury, H.-H. Kim, A.B. Murphy, W.F. Schneider, T. Nozaki, J.C. Hicks, A. Rousseau, F. Thevenet, A. Khacef, M. Carreon, The 2020 plasma catalysis roadmap, J. Phys. d: Appl. Phys. 53 (2020) 443001.
[6] S. Yang, H. Yang, J. Yang, H. Qi, J. Kong, Z. Bo, X. Li, J. Yan, K. Cen, X. Tu, Three-dimensional hollow urchin α-MnO_2 for enhanced catalytic activity towards toluene decomposition in post-plasma catalysis, Chem. Eng. J. 402 (2020) 126154–126164.
[7] J. Liu, H. Wang, L. Wang, P. Jian, X. Yan, Phase-dependent catalytic performance of MnO_2 for solvent-free oxidation of ethybenzene with molecular oxygen, Appl. Catal. B: Environ. 305 (2022) 121050–121058.
[8] W. Yang, Z.a. Su, Z. Xu, W. Yang, Y. Peng, J. Li, Comparative study of α-, β-, γ- and δ-MnO_2 on toluene oxidation: Oxygen vacancies and reaction intermediates, Appl. Catal. B: Environ. 260 (2020) 118150–118159.
[9] J. Ji, X. Lu, C. Chen, M. He, H. Huang, Potassium-modulated δ-MnO_2 as robust catalysts for formaldehyde oxidation at room temperature, Appl. Catal. B: Environ. 260 (2020) 118210–118221.
[10] Y. Qin, Y. Liu, Y. Zhang, Y. Gu, Y. Lian, Y. Su, J. Hu, X. Zhao, Y. Peng, K. Feng, J. Zhong, M.H. Rummeli, Z. Deng, Ru-substituted MnO_2 for accelerated water oxidation: The feedback of strain-induced and polymorph-dependent structural changes to the catalytic activity and mechanism, ACS Catal. 13 (2022) 256–266.
[11] G. Zhu, W. Zhu, Y. Lou, J. Ma, W. Yao, R. Zong, Y. Zhu, Encapsulate α-MnO_2 nanofiber within graphene layer to tune surface electronic structure for efficient ozone decomposition, Nat. Commun. 12 (2021) 4152.
[12] H. Usui, S. Suzuki, Y. Domi, H. Sakaguchi, Impacts of MnO_2 crystal structures and Fe doping in those on photoelectrochemical charge-discharge properties of TiO_2/MnO_2 composite electrodes, ACS Sustain. Chem. Eng. 8 (2020) 9165–9173.
[13] X. Zhu, S. Zhang, Y. Yang, C. Zheng, J. Zhou, X. Gao, X. Tu, Enhanced performance for plasma-catalytic oxidation of ethyl acetate over $La_{1-x}Ce_xCoO_{3+\delta}$ catalysts, Appl. Catal. B: Environ. 213 (2017) 97–105.
[14] X. Zheng, J. Cai, Y. Cao, L. Shen, Y. Zheng, F. Liu, S. Liang, Y. Xiao, L. Jiang, Construction of cross-linked δ-MnO_2 with ultrathin structure for the oxidation of H_2S: Structure-activity relationship and kinetics study, Appl. Catal. B: Environ. 297 (2021) 120402–120417.
[15] P. Wu, S. Dai, G. Chen, S. Zhao, Z. Xu, M. Fu, P. Chen, Q. Chen, X. Jin, Y. Qiu, S. Yang, D. Ye, Interfacial effects in hierarchically porous α-MnO_2/Mn_3O_4 heterostructures promote photocatalytic oxidation activity, Appl. Catal. B: Environ. 268 (2020) 118418–118427.
[16] Q. Zhao, Y. Zhang, Q. Liu, C. Song, X. Lu, J. Ma, L. Wang, H. He, Boosting the catalytic performance of colatile organic compound oxidation over platelike MnO_2/CoAlO catalyst by weakening the Co–O bond and accelerating oxygen activation, ACS Catal. 13 (2023) 1492–1502.
[17] S. Ndayiragije, Y. Zhang, Y. Zhou, Z. Song, N. Wang, T. Majima, L. Zhu, Mechanochemically tailoring oxygen vacancies of MnO_2 for efficient degradation of tetrabromobisphenol A with peroxymonosulfate, Appl. Catal. B: Environ. 307 (2022) 121168–121183.
[18] W. Chung, D. Mei, X. Tu, M. Chang, Removal of VOCs from gas streams via plasma and catalysis, Catalysis Reviews. 61 (2018) 270–331.
[19] M. Hu, Z. Yao, K.N. Hui, K.S. Hui, Novel mechanistic view of catalytic ozonation of gaseous toluene by dual-site kinetic modelling, Chem. Eng. J. 308 (2017) 710–718.
[20] E. Rezaei, J. Soltan, EXAFS and kinetic study of MnO_x/γ-alumina in gas phase catalytic oxidation of toluene by ozone, Appl. Catal. B: Environ. 148–149 (2014) 70–79.
[21] Y. Liu, P. Zhang, J. Zhan, L. Liu, Heat treatment of $MnCO_3$: An easy way to obtain efficient and stable MnO_2 for humid O_3 decomposition, Appl. Surf. Sci. 463 (2019) 374–385.
[22] Y. Liu, H. Zhou, R. Cao, X. Liu, P. Zhang, J. Zhan, L. Liu, Facile and green synthetic strategy of birnessite-type MnO_2 with high efficiency for airborne benzene removal at low temperatures, Appl. Catal. B: Environ. 245 (2019) 569–582.
[23] D.W. Stephan, The broadening reach of frustrated Lewis pair chemistry, Science. 354 (2016) 479–484.
[24] P. Lu, L. Ye, X. Yan, P. Fang, X. Chen, D. Chen, C. Cen, Impact of toluene poisoning on MnCe/HZSM-5 SCR catalyst, Chem. Eng. J. 414 (2021) 128838.
[25] L. Ye, P. Lu, X. Chen, P. Fang, Y. Peng, J. Li, H. Huang, The deactivation mechanism of toluene on MnO_x-CeO_2 SCR catalyst, Appl. Catal. B: Environ. 277 (2020) 119257–119265.
[26] Y. Guo, X. Hong, Y. Su, W. Luo, R. Yu, J. Wu, E.J.M. Hensen, L. Mai, Y. Cao, Sub-nanometer confined ions and solvent molecules intercalation capacitance in microslits of 2D materials, Small. 17 (2021) 2104649.
[27] Q. Yang, W. Xu, S. Gong, G. Zheng, Z. Tian, Y. Wen, L. Peng, L. Zhang, Z. Lu, L. Chen, Atomically dispersed Lewis acid sites boost 2-electron oxygen reduction activity of carbon-based catalysts, Nat. Commun. 11 (2020) 5478.
[28] Y. Ha, M. Mu, Q. Liu, N. Ji, C. Song, D. Ma, Mn-MIL-100 heterogeneous catalyst for the selective oxidative cleavage of alkenes to aldehydes, Catal. Commun. 103 (2018) 51–55.
[29] B. Chen, B. Wu, L. Yu, M. Crocker, C. Shi, Investigation into the catalytic roles of various oxygen species over different crystal phases of MnO_2 for C_6H_6 and HCHO oxidation, ACS Catal. 10 (2020) 6176–6187.
[30] K. Ham, J. Lee, K. Lee, J. Lee, Boosting the oxygen evolution reaction performance of wrinkled $Mn(OH)_2$ via conductive activation with a carbon binder, J. Energy. Chem. 71 (2022) 580–587.
[31] Q. Chen, J. Jin, M. Song, X. Zhang, H. Li, J. Zhang, G. Hou, Y. Tang, L. Mai, L. Zhou, High-energy aqueous ammonium-ion hybrid supercapacitors, Adv. Mater. 34 (2022) 2107992.
[32] H. Tang, W. Chen, N. Li, Z. Hu, L. Xiao, Y. Xie, L. Xi, L. Ni, Y. Zhu, Layered MnO_2 nanodots as high-rate and stable cathode materials for aqueous zinc-ion storage, Energy Storage Mater. 48 (2022) 335–343.
[33] Y.K. Hsu, Y.C. Chen, Y.G. Lin, L.C. Chen, K.H. Chen, Reversible phase transformation of MnO_2 nanosheets in an electrochemical capacitor investigated by in situ Raman spectroscopy, Chem. Commun. 47 (2011) 1252–1254.
[34] S. Wu, H. Liu, Z. Huang, H. Xu, W. Shen, O-vacancy-rich porous MnO_2 nanosheets as highly efficient catalysts for propane catalytic oxidation, Appl. Catal. B: Environ. 312 (2022) 121387–121398.
[35] L. Chen, C. Zhang, Y. Li, C.-R. Chang, C. He, Q. Lu, Y. Yu, P. Duan, Z. Zhang, R. Luque, Hierarchically hollow MnO_2@CeO_2 heterostructures for NO oxidation: Remarkably promoted activity and SO_2 tolerance, ACS Catal. 11 (2021) 10988–10996.
[36] Y. Wang, X. Li, Q. Zhou, B. Wang, T. Qi, G. Liu, Z. Peng, K. Zhou, Observation of sodium titanate and sodium aluminate silicate hydrate layers on diaspore particles in high-temperature Bayer digestion, Hydrometallurgy. 192 (2020) 105255.
[37] J. Zhang, W. Wang, B. Li, Enabling high sodium storage performance of micron-sized Sn_4P_3 anode via diglyme-derived solid electrolyte interphase, Chem. Eng. J. 392 (2020) 123810.
[38] Y. Chen, S. Zhang, X. Xu, P. Yao, T. Li, G. Wang, G. Gong, Y. Li, O. Deng, Effects of surfactants on low-molecular-weight organic acids to wash soil zinc, Environ. Sci. Pollut. Res. Int. 23 (2016) 4629–4638.
[39] C.-K. Lee, C.-C. Wang, L.-C. Juang, M.-D. Lyu, S.-H. Hung, S.-S. Liu, Effects of sodium content on the microstructures and basic dye cation exchange of titanate nanotubes, Colloids Surf. A. 317 (2008) 164–173.
[40] M. Race, R. Marotta, M. Fabbricino, F. Pirozzi, R. Andreozzi, M. Guida, A. Siciliano, Assessment of optimal conditions for the restoration and recovery of agricultural soil, J. Hazard. Mater. 373 (2019) 801–809.
[41] C. Wang, J. Chen, Q. Li, S. Su, H. Jia, H. He, Unveiling the position effect of Ce within layered MnO_2 to prolong the ambient removal of indoor HCHO, Environ. Sci. Technol. 57 (2023) 4598–4607.
[42] J. Wang, P. Zhang, J. Li, C. Jiang, R. Yunus, J. Kim, Room-temperature oxidation of formaldehyde by layered manganese oxide: Effect of water, Environ. Sci. Technol. 49 (2015) 12372–12379.
[43] L. Liu, Y.C. Wu, L. Huang, K. Liu, B. Duployer, P. Rozier, P.L. Taberna, P. Simon, Alkali ions pre-intercalated layered MnO_2 nanosheet for zinc-ions storage, Adv. Energy Mater. 11 (2021) 2101287.
[44] Y.F. Li, S.C. Zhu, Z.P. Liu, Reaction network of layer-to-tunnel transition of MnO_2, J. Am. Chem. Soc. 138 (2016) 5371–5379.
[45] Y. Guo, M. Wen, S. Song, Q. Liu, G. Li, T. An, Enhanced catalytic elimination of typical VOCs over $ZnCoO_x$ catalyst derived from in situ pyrolysis of ZnCo bimetallic zeolitic imidazolate frameworks, Appl. Catal. B: Environ. 308 (2022) 121212–121220.
[46] S. Bailleul, I. Yarulina, A.E.J. Hoffman, A. Dokania, E. Abou-Hamad, A. D. Chowdhury, G. Pieters, J. Hajek, K. De Wispelaere, M. Waroquier, J. Gascon, V. Van Speybroeck, A supramolecular view on the cooperative role of bronsted and Lewis acid sites in zeolites for methanol conversion, J. Am. Chem. Soc. 141 (2019) 14823–14842.
[47] S. Alejandro, H. Valdes, M.H. Manero, C.A. Zaror, Oxidative regeneration of toluene-saturated natural zeolite by gaseous ozone: the influence of zeolite chemical surface characteristics, J. Hazard. Mater. 274 (2014) 212–220.
[48] T. Chang, J. Lu, Z. Shen, Y. Huang, D. Lu, X. Wang, J. Cao, R. Morent, Simulation and optimization of the post plasma-catalytic system for toluene degradation by a hybrid ANN and NSGA-II method, Appl. Catal. B: Environ. 244 (2019) 107–119.
[49] C. Chen, M. Kosari, C. He, M. Ma, M. Tian, Z. Jiang, R. Albilali, Realizing toluene deep mineralization by coupling nonthermal plasma and nitrogen-enriched hollow hybrid carbon, ACS Appl. Mater. Interfaces. 14 (2022) 990–1001.
[50] T. Chang, Z. Shen, Y. Huang, J. Lu, D. Ren, J. Sun, J. Cao, H. Liu, Post-plasma-catalytic removal of toluene using MnO_2-Co_3O_4 catalysts and their synergistic mechanism, Chem. Eng. J. 348 (2018) 15–25.
[51] B. Wang, C. Chi, M. Xu, C. Wang, D. Meng, Plasma-catalytic removal of toluene over CeO_2-MnO_x catalysts in an atmosphere dielectric barrier discharge, Chem. Eng. J. 322 (2017) 679–692.
[52] X. Li, S. Wang, X. Zhang, D. Mei, Y. Xu, P. Yu, Y. Sun, Nonthermal plasma catalysis enhances simultaneous removal of toluene and ozone over TiO_2@ZIF-8, J. Cleaner Prod. 332 (2022) 130107–130118.
[53] X. Liu, J. Liu, J. Chen, F. Zhong, Mn_2O_3/γ-Al_2O_3 catalysts synergistic double dielectric barrier discharge (DDBD) degradation of toluene, ethyl-acetate and acetone, Chemosphere. 284 (2021) 131299.
[54] B. Zhu, L. Zhang, M. Li, Y. Yan, X. Zhang, Y. Zhu, High-performance of plasma-catalysis hybrid system for toluene removal in air using supported Au nanocatalysts, Chem. Eng. J. 381 (2020) 122599.
[55] X. Zhang, B. Ren, Y. Xu, X. Li, P. Yu, Y. Sun, H. Zheng, Catalytic oxidation of toluene in air using manganese incorporated catalyst by non-thermal plasma system, Sep. Purif. Technol. 257 (2021) 117973.
[56] J. Chen, C. Sun, Z. Huang, F. Qin, H. Xu, W. Shen, Fabrication of functionalized porous silica nanocapsules with a hollow structure for high performance of toluene adsorption-desorption, ACS Omega. 5 (2020) 5805–5814.
[57] Y. Shao, S. Ba, K. Sun, G. Gao, M. Fan, J. Wang, H. Fan, L. Zhang, X. Hu, Selective production of γ-valerolactone or 1,4-pentanediol from levulinic acid/esters over Co-based catalyst: Importance of the synergy of hydrogenation sites and acidic sites, Chem. Eng. J. 429 (2022) 132433.
[58] F. Meng, R. Wang, H. Huang, S. Gong, Q. Li, S. Zhang, C. Ma, C. Li, J. Du, Lewis acid-catalyzed tandem cyclization of in situ generated o-quinone methides and arylsulfonyl hydrazides for a one-pot entry to 3-sulfonylbenzofurans, Org. Chem. Front. 6 (2019) 3929–3933.

[59] G. Yang, S. Shang, B. Yu, C. Hu, Ce(III)-Containing tungstotellurate(IV) with a sandwich structure: an efficient Lewis acid-base catalyst for the condensation cyclization of 1,3-diketones with hydrazines/hydrazides or diamines, Inorge. Chem. Front. 5 (2018) 2472–2477.
[60] G.M. Kiefl, T. Gulder, alpha-Functionalization of ketones via a nitrogen directed oxidative umpolung, J. Am. Chem. Soc. 142 (2020) 20577–20582.
[61] K. Vikrant, K.-H. Kim, V. Kumar, D.A. Giannakoudakis, D.W. Boukhvalov, Adsorptive removal of an eight-component volatile organic compound mixture by Cu-, Co-, and Zr-metal-organic frameworks: Experimental and theoretical studies, Chem. Eng. J. 397 (2020) 125391.
[62] T. Wang, S. Chen, H. Wang, Z. Liu, Z. Wu, In-plasma catalytic degradation of toluene over different MnO_2 polymorphs and study of reaction mechanism, Chin. J. Catal. 38 (2017) 793–803.
[63] Z. Bo, S. Yang, J. Kong, J. Zhu, Y. Wang, H. Yang, X. Li, J. Yan, K. Cen, X. Tu, Solar-enhanced plasma-catalytic oxidation of toluene over a bifunctional graphene fin foam decorated with nanofin-like MnO_2, ACS Catal. 10 (2020) 4420–4432.
[64] A. Al-Abduly, P. Christensen, A. Harvey, The characterization of a packed bed plasma reactor for ozone generation, Plasma Sources Sci. Technol. 29 (2020) 035002.
[65] J. Ree, Y.H. Kim, H.K. Shin, Collision-induced CH bond dissociation in highly excited toluene, Chem. Phys. Lett. 394 (2004) 250–256.
[66] L. Liu, J. Dai, S. Das, Y. Wang, H. Yu, S. Xi, Z. Zhang, X. Tu, Plasma-catalytic CO_2 reforming of toluene over hydrotalite-derived NiFe/(Mg, Al)O_x catalysts, JACS Au. 3 (2023) 785–800.